Solar Energy 299 (2025) 113747

Contents lists available at ScienceDirect

Solar Energy

journal homepage: www.elsevier.com/locate/solener

A life-cycle economic comparison of distributed photovoltaic power stations coupled with integrated electrolysis systems: optimization of directly and indirectly coupled modes

Zunbo Wang [a,c], Yong He [a,b,*], Wanzhen Wang [c], Zhongtao Liao [c], Wubin Weng [a,b], Zhihua Wang [a,b], Shengtao Qian [a]

[a] *State Key Laboratory of Clean Energy Utilization, Zhejiang University, Hangzhou 310027, China*
[b] *Qingshanhu Energy Research Center, Zhejiang University, Hangzhou, 311300, China*
[c] *PetroChina Yumen Oilfield, Jiuquan 735008, China*

ARTICLE INFO

Keywords:
Distributed photovoltaic power stations
Integrated electrolysis systems
Directly coupled
Levelized cost of hydrogen
Life cycle economic analysis

ABSTRACT

Integrating distributed photovoltaic (PV) systems for hydrogen production has gained an increasing research attention as a way to improve solar energy utilization and enhance energy storage. However, economic assessments of different technological routes for PV-powered electrolysis remain limited. This study fills this gap by evaluating the life cycle economic feasibility of distributed PV stations coupled with integrated electrolysis systems (IES). The main contribution of this work is the comprehensive analysis of both direct and indirect coupling of PV and electrolysis systems, providing new insights into the cost-effectiveness and long-term potential of solar-driven hydrogen production. For the direct coupling of PV power generation with proton exchange membrane (PEM) electrolyzers, MATLAB/Simulink is used for simulation experiments. For indirect coupling, experimental data from distributed PV power stations and PEM and alkaline (ALK) electrolyzers in practical application at the Yumen Oilfield are used. The results show that the Levelized Cost of Hydrogen (LCOH) for directly coupled PEM is € 2.93–2.99/kg, for indirectly coupled PEM, it is € 4.47–4.65/kg, and for indirectly coupled ALK, it is € 2.55–2.68/kg. These findings are significant for the economic analysis of PV panels directly coupled with PEM and distributed PV hydrogen production systems.

1. Introduction

As solar energy continues to play a central role in the transition to sustainable energy systems, its efficient utilization has become a key area of research. Research by Yasmeen et al. [1] explored the adequacy of photovoltaic (PV) power at various income levels in China, highlighting the regional disparities and their implications for solar energy deployment. In addition, Boruah and Chandel [2] provided a comprehensive analysis of rooftop grid-connected solar PV systems with battery energy storage, demonstrating how such setups enhance energy security and improve grid resiliency. Dumlao and Ogata [3] focused on the local consumption of solar energy in Japan, examining the role of energy demand in residential and small-scale solar projects. PV technology has advanced significantly, offering a reliable and scalable renewable energy source. Li et al. [4] conducted a techno-economic analysis of a hybrid energy system combining wind, PV, electrolysis, and battery storage for both power and hydrogen generation, providing insights into its economic viability. However, the intermittent nature of solar power presents challenges for grid stability and energy management. To address these challenges, researchers have proposed various technical approaches to enhance the PV system's energy conversion efficiency and ensure grid power supply stability. Miao et al. [5] analyzed the levelized cost of long-distance transportation of hydrogen in China, which is critical for understanding the infrastructure challenges related to solar-driven hydrogen production. Park et al. [6] proposed strategies for balancing economic viability with reliability, addressing the supply–demand volatility inherent in solar power. Antonanzas et al. [7] reviewed PV power forecasting methods, highlighting the role of accurate predictions in optimizing PV grid integration. Finally, Haupt et al. [8] investigated how blending distributed PV and demand load forecasts can improve the accuracy and reliability of energy management in solar power systems.

---

* Corresponding author.
E-mail address: heyong@zju.edu.cn (Y. He).

https://doi.org/10.1016/j.solener.2025.113747
Received 20 March 2025; Received in revised form 2 June 2025; Accepted 28 June 2025

A promising method among these approaches is integrating PV power generation with electrolysis for hydrogen production [9]. By converting excess solar electricity into hydrogen, these systems provide a means of long-term energy storage, allowing solar energy to be utilized even when direct generation is not available [10]. This integration not only enhances the efficiency of solar power utilization but also contributes to decarbonization efforts by enabling clean hydrogen production [11]. As a result, distributed PV power stations coupled with integrated electrolysis systems (IES) have attracted increasing interest from both academia and industry. For example, Atiz and Karakilçik [12] assessed hydrogen generation and efficiency in PV-PEM systems, while Fu et al. [13] explored the integration of PV/T and ASHP systems for energy balance and grid stability. Other research by Mas et al. [14] focused on optimizing the size of PV-ALK systems, and Mas et al. [15] examined the use of sliding mode control in these systems. Zhang et al. [16] compared hydrogen production from onshore and offshore wind, and Bentoumi et al. [17] investigated green hydrogen production using solar power plants in desert climates. However, while the potential of these systems is well recognized, their large-scale economic feasibility remains an area of ongoing research. Understanding cost and optimizing system performance are key to advancing solar-driven hydrogen production and its role in future energy systems.

Despite the advancements, there are significant knowledge gaps in the comprehensive economic analysis of different PV-IES configurations. Farid Sayedin [18] et al. conducted an optimization analysis of both the technical and economic performance of the system, finding that climatic conditions significantly impact the levelized cost of hydrogen (LCOH). Mengxiang Zhu [19] et al. established a simulation model of large-scale centralized PV power generation and hydrogen production system coupling by using MATLAB software and carried out real-time simulation. Their results provided an economic reference for the research of centralized green hydrogen production systems. Previous studies have largely focused on either the technical optimization of centralized PV hydrogen generation systems or the economic evaluation of small-scale systems, with limited research addressing large-scale, distributed PV systems coupled with electrolysis. Diederik Coppitters [20] et al. used meteorological data from various locations worldwide to study the economic indicators of scaling up hydrogen production projects, highlighting the importance of scale for economic efficiency. In 2024, Tuyen Nguyen Duc [21] et al. conducted an experiment on direct coupling systems, demonstrating that the scale of direct coupling systems can now reach 1 MW. Moreover, existing studies on the economic performance of direct and indirect coupling modes are scarce, and the life-cycle assessment of these systems, which considers all stages from investment to operation, is often overlooked. In a 2023 review article on direct coupling systems, Long Phan Van [22] et al. summarized nearly 20 papers on the subject. Of these, 17 papers focused on optimizing the technical aspects of the system, while only 3 papers aimed at optimizing the economic aspects. T. Tani et al. [23] (2000) highlighted the PV/electrolyzers (ELY) cost ratios' significance. However, their conclusions were limited by the inadequate power supply (3.4 V/27.45A). Diederik Coppitters et al. [18] (2016) utilized a 72 × MSX-60 PV array (theoretical power ~4.32 kW), with the optimized system yielding hydrogen at € 6.4 ± 0.74/kg. Farid Sayedin et al. [20] (2019) found out that the solar-to-hydrogen efficiency of the optimal systems regarding these cities are different based on the solution scenarios, the characteristics of PV output power, and the configuration of optimal ELY configuration and placement. These studies focus solely on PV-single ELY coupling, without examining the economics of different PV-IES connection methods (direct/indirect) in distributed systems or providing sufficient real-world experimental validation.

To address these gaps, this study adopts a life-cycle approach to evaluate the economic performance of three coupling routes: directly coupled PV-PEM systems, indirectly coupled PV-PEM systems, and indirectly coupled PV-ALK systems. The direct coupling system is optimized using the multi-objective particle swarm optimization algorithm (MOPSO) to minimize the LCOH. The indirect coupling system utilizes experimental data from a 5 MW PV power plant, PEM, and ALK, as applied in the Yumen Oilfield. The MOPSO algorithm is designed to minimize the LCOH by balancing multiple objectives simultaneously [24]. This algorithm has demonstrated effectiveness across multiple domains, including hydrogen production optimization [25], multi-objective energy allocation [26], and distributed PV systems [27], as will be discussed in detail in the methodology section.

The main contributions of this study are as follows:

Coupling Systems Optimization: A method for optimizing large-scale PV systems directly coupled with PEM using MOPSO has been proposed, which minimizes the LCOH and provides a more cost-effective and scalable solution for PV driven hydrogen production.

Comprehensive Economic Comparison: A detailed life cycle economic analysis is presented, providing new insights into the cost-effectiveness of different coupling routes: directly PV-PEM, indirectly PV-PEM, and indirectly PV-ALK, which have not been fully explored in previous research, particularly in terms of long-term economic feasibility.

Feasibility insight: Provides important insights into the economic feasibility of distributed PV hydrogen systems, especially in remote and off-grid areas. By analyzing investment costs, operating expenses, and hydrogen production, the understanding gap on how to integrate distributed systems into the actual energy market has been addressed, providing a pathway for sustainable energy deployment.

The structure of the paper is distributed as follows: Section 2 states the System Overview and Site Selection. Section 3 describes the System Modeling and optimization strategy. The final results and discussion are illustrated in Section 4. Concrete conclusions and future prospects are drawn in Section 5.

2. System overview and site selection

2.1. System configuration and description

This study conducts an economic analysis comparing two configurations: direct and indirect coupling. For experimental validation, the direct coupling system is simulated using MATLAB/Simulink, while the indirect coupling system is tested with practical hardware, including the distributed PV power station, PEM, and ALK electrolyzers in the real world of Yumen Oilfield. Fig. 1 presents the experimental setup of the PV-IES hydrogen production facility, demonstrating both simulation and physical validation.

A DC coupling route is employed to conduct direct coupling experiments between PV power stations and IES. The experimental system is configured with a 5 MW PV power generation field (composed of five 1 MW PV power generation fields in series), five sets of 200 Nm^3/h PEM hydrogen production containers, and auxiliary devices for compression and storage. Every PEM hydrogen production container includes a PEM electrolyzer and a set of temperature swing adsorption (TSA) devices. The PV stations and IES operate independently, with coordinated intelligent control to ensure that hydrogen production power follows PV power fluctuations. The size of every single PV field is optimized to minimize the LCOH, and the overall system efficiency is calculated at the point of lowest LCOH. The series–parallel size of the PV fields is selected considering the inherent volatility and intermittency of PV power generation, and reasonable configurations are made based on the overall economic evaluation of the hydrogen production system. For indirect coupling experiments between PV power stations and IES, an AC coupling route is used. The 5MWp PV power generation field is matched with five sets of 200 Nm^3/h PEM hydrogen production containers or a 1000Nm^3/h ALK electrolyzer with additional gas–liquid separation and TSA devices. The auxiliary facilities, such as compressors and storage tanks, are shared by both direct and indirect coupling systems. The

Fig. 1. Experimental and simulation setup of the PV-hydrogen production system (direct coupling: Simulink model; indirect coupling: PEM/ALK electrolyzer hardware test in Yumen Oilfield).

LCOH is estimated based on field experimental data and investment conditions. The life cycle assessment boundaries for PV hydrogen production include six stages: purchase and transportation of PV panels and equipment; construction and installation of PV panels and equipment; PV power generation; purchase and transportation of hydrogen production equipment; construction and installation of hydrogen production equipment; and water electrolysis hydrogen production. Finally, a comparative analysis of the LCOH for three routes of distributed PV hydrogen production is conducted.

Gansu Province boasts abundant solar energy resources, particularly in regions such as the Hexi Corridor, where solar radiation levels reach 5800 MJ/m2 annually. Yumen City, located at 97°39′4″ E longitude and 39°43′15″ N latitude, experiences varying solar radiation throughout the seasons. Summer exhibits the highest radiation, while winter sees the lowest levels. Additionally, spring radiation surpasses that of autumn. Situated at an altitude of approximately 2000–2250 m, Yumen City belongs to the plateau area (Obtained from the China Meteorological Science Data Sharing Service Network (MSSN) https://data.cma.cn/). At higher altitudes, air density decreases, resulting in less absorption and scattering of irradiance. Specifically, Yumen City experiences an annual representative total solar irradiance of 1704 kWh/m^2, with scattered radiation measuring 605 kWh/m^2. The average annual temperature is 2.7 °C, accompanied by an average wind speed of 2.6 m/s. Table 1 delineates the representative annual climate data (irradiance, temperature, wind speed) of Yumen City in Solar GIS data sources, where GHI is Global Horizontal Irradiance and DNI is Direct Normal Irradiance. The above data are obtained from Solar GIS (https://solargis.com/cn/resources/free-maps-and-gis-data?locality=china), a high-resolution (250 m) solar resource and climate assessment database developed by Geo Model Solar based on satellite remote sensing data and GIS (Geographic Information System) technology and scientific algorithms.

Table 1
Representative annual climate data (irradiance, temperature, wind speed) in Yumen city.

Month	1	2	3	4	5	6
GHI (kWh/m^2)	80	96	137	172	208	201
DNI (kWh/m^2)	152	143	160	184	198	187
Temperature (°C)	−14.9	−8.9	−2.2	5.3	11.1	15.6
Wind Speed (m/s)	2.4	2.7	3.1	3.5	2.8	2.6
Month	7	8	9	10	11	12
GHI (kWh/m^2)	197	183	154	123	85	70
DNI (kWh/m^2)	177	195	160	174	140	134
Temperature (°C)	17	15.2	9.8	2.9	−5.2	−13.2
Wind Speed (m/s)	2.5	2.3	2.2	2.2	2.5	2.3

2.2. PV system description

The experimental apparatus encompasses two primary conversion processes: the conversion of solar energy to electrical energy (STE) and the conversion of electrical energy to hydrogen (ETH). The conversion of STE is accomplished by the PV system. The direct coupling PV system converts solar energy into DC electricity. To avoid significant energy losses during high-power DC transmission, the system comprises five 1 MW PV fields forming a 5 MW PV power station. In contrast, the indirect coupling PV system directly employs a 5 MW PV power station to convert solar energy into AC electricity. The conversion of ETH is characterized by the use of electrolyzers, supplemented by gas–liquid separation, purification, compression, and storage devices.

The design of this experimental apparatus takes into account various factors, including module efficiency, technological maturity, module production capacity, and the local wind speed and solar radiation in Yumen City. The PV system employs a combination of P-type single-crystal high-efficiency half-cell Passivated Emitter and Rear Cell (PERC) double-sided 540Wp modules and fixed brackets. The PV panels are installed and operated at a fixed inclination angle of 35°, a PV panel azimuth angle of 0°, and a distance of 11.9 m between two rows of arrays. The PV panels have a lifespan of 20 years. Table 2 delineates the detailed parameters of the PV panels used in this study, which are obtained from the PV panel manufacturer. The selected PV modules are LONGI's 540Wp monocrystalline silicon PV panels of a certain model.

2.3. Hydrogen production system description

In this study, the hydrogen production system employs two types of currently mature technologies: ALK and PEM electrolyzers [28–30].

The ALK electrolyzer has a capacity of 1000 Nm^3/h, with a rated operating voltage of 496 V and a rated operating current of 10712A. It is equipped with gas–liquid separation and TSA devices and uses a 30 % KOH solution as the hydrogen production feedstock. A single PEM electrolyzer has a capacity of 200 Nm^3/h and is configured with a dual-stack structure. Each stack consists of two series-connected 50 Nm^3/h PEM electrolyzers, resulting in a total capacity of 200 Nm^3/h for the PEM electrolyzer. Due to the small footprint of the PEM electrolyzer, it is designed as a mobile water electrolysis system. This means that all equipment (electrolysis, purification) and process pipelines (hydrogen, oxygen, instrument air, nitrogen, circulating cooling water, etc.) of the water electrolysis system are arranged on several movable or transportable chassis or bases, thereby reducing investment and construction costs. The deionized water required for the PEM electrolyzers first enters the water tank and then is pumped into the PEM electrolyzers by a circulation pump. Under the electrolysis of direct current, hydrogen and oxygen are produced. The oxygen flows back to the water tank with the return water on the oxygen side and is discharged to the outdoor atmosphere after passing through the water seal of the water tank. The hydrogen enters the purification device, where it is purified by palladium catalysis and molecular sieves to obtain hydrogen with a purity of 99.999 %.

3. System modeling

This section first provides a detailed description of the modeling process for the PV, hydrogen production, and auxiliary systems used for the direct coupling system, followed by a description of the optimization algorithms and evaluation metrics. The experiments in this study are optimized with the goal of system economic efficiency, aiming to minimize the LCOH.

3.1. PV system modeling

Most mathematical analyses of PV system components employ the single-diode model, which calculates the current–voltage relationship based on incident solar irradiance and the surface temperature of the panels. In this study, the PV system model is configured with two input signals: the first input signal is the control signal for the irradiance applied to the PV panels, measured in W/m^2, and the second input signal is the control signal for the temperature of the PV panels, measured in °C. The relationship between the operating current (I_{pv}) and the operating voltage (V_{pv}) within the PV system model is given by the following equations [20]:

Table 2
Typical specification of the PV panel.

Quantity	Unit	Value
Maximum power	Wp	540.2
Open circuit voltage	V	49.5
Short circuit current	A	13.85
Component conversion efficiency	%	21.1
Maximum power voltage	V	41.65
Maximum power current	A	12.97
Temperature coefficient of maximum power	%/°C	−0.35
Temperature coefficient of open circuit voltage	%/°C	−0.28
Temperature coefficient of short circuit current	%/°C	+0.05

$$I_{\mathrm{PV}} = I_L - I_0 \left\{ \exp\left[\frac{V_{PV} + I_{PV} * R_s}{\alpha_{\mathrm{ref}} \left(\frac{T_c}{T_{c,\mathrm{ref}}} \right)} \right] - 1 \right\} \tag{1}$$

$$I_L = \frac{G_T}{G_{T,ref}} * \left[I_{L,ref} + \mu_{I,sc} * \left(T_c - T_{c,ref} \right) \right] \tag{2}$$

$$I_0 = I_{0,ref} \left(\frac{T_c}{T_{c,ref}} \right)^3 * \exp\left[\left(\frac{e_{gap} * N_{cell}}{\alpha_{ref}} \right) * \left(1 - \frac{T_{c,ref}}{T_c} \right) \right] \tag{3}$$

where I_o, I_L denote the light current and diode reverse saturation current respectively, R_s the series resistance, α_{ref} the reference curve fitting parameter, G_T, $G_{T,ref}$ the solar irradiance and reference solar irradiance, T_c, $T_{c,ref}$ the panel temperature and reference temperature, $I_{o,ref}$, $I_{L,ref}$ the diode reverse saturation reference current and short circuit current respectively and e_{gap} the band gap of Si, N_{cell} the number of cells. The *ref* indicates the reference conditions of G = 1000 W/m^2 and T = 25 °C.

The interrelationship between the current and voltage at both ends of the system is elucidated in the following equation [20], where (N_s) and (N_p) represent the number of series and parallel PV panels, respectively.

$$I_{PV} * N_s = I_{ELY} \tag{4}$$

$$V_{PV} * N_p = V_{ELY} \tag{5}$$

3.2. Hydrogen production system modeling

This study employs a dynamic PEM electrolyzer simulation model that considers multiphase flow, based on principles of conservation and electrode reaction kinetics [31,32]. Additionally, this paper enhances the original dynamic model by incorporating the limitations of saturation pressure on the partial pressures of water vapor at the anode and cathode, as well as improvements to account for the displacement of air by water from the electrode chambers before the ELY begins formal operation, thereby making the dynamic model more comprehensive.

During the reaction, water undergoes decomposition at the anode module of the electrolytic cell, resulting in an oxygen evolution reaction (OER). The protons generated from this decomposition traverse the proton exchange membrane to reach the cathode module, where a hydrogen evolution reaction (HER) occurs. The rates of OER and HER can be expressed as [33,34]:

$$N_{O_2} = N_{O_2\mathrm{ai}} - N_{O_2\mathrm{ao}} + N_{O_2\mathrm{g}} \tag{6}$$

$$N_{H_2Oa} = N_{H_2Oai} - N_{H_2Oao} - N_{H_2Oeod} - N_{H_2Odiff} \tag{7}$$

$$N_{H_2} = N_{H_2\mathrm{ci}} - N_{H_2\mathrm{co}} + N_{H_2\mathrm{g}} \tag{8}$$

$$N_{H_2Oc} = N_{H_2Oco} - N_{H_2Oeos} + N_{H_2Odiff} \tag{9}$$

where N_{O2}, N_{H2} is the total amount of oxygen and hydrogen, N_{H2Oa}, N_{H2Oc} the amount of anode and cathode water, N_{H2ai}, N_{H2ao}, N_{H2Oai}, N_{H2Oao}, N_{H2ci}, N_{H2co}, N_{H2Oci}, N_{H2Oco} the amount of oxygen, water entering and exiting the anode and cathode respectively, N_{O2g}, N_{H2g} the amount of oxygen and hydrogen generated in the electrolytic cell, $N_{H2Odiff}$ and N_{H2Oeod} the amount of water passing through the membrane through diffusion and osmosis.

The cumulative gas pressure engendered by the anode and cathode, in conjunction with the partial pressure of H_2O, constitutes the total pressure within both the anode and cathode compartments. The partial pressure of H_2O is constrained to not surpass the saturation pressure at the prevailing operational temperature. Prior to the initiation of the electrolyzer's operation, the air residing within the anode chamber is expelled concomitantly with water. The quantitative interrelationship among these variables is delineated by Eq. (10) [35] and Eq. (11) [35]. This elucidates the intricate dynamics governing the system under study.

$$P_a = P_{O_2} + P_{H_2Oa} \tag{10}$$

$$P_c = P_{H_2} + P_{H_2Oc} \tag{11}$$

Water typically traverses the membrane through diffusion and electro-osmosis. The quantities $N_{H2Odiff}$ and N_{H2Oeos} can be calculated using the following equations [35]:

$$N_{H_2Oeos} = n_d M_{H_2O} I_{ELY} A_{cell}/F \tag{12}$$

$$N_{H_2Odiff} = D_{\omega}\left(\frac{C_{\varpi c} - C_{\varpi a}}{t_{me}}\right) M_{H_2O} A_{cell} \tag{13}$$

where $C_{\omega c}$, $C_{\omega a}$ is the concentration of water on the surface of the anode and cathode membrane, D_{ω} is the diffusion coefficient of water in the proton exchange membrane, A_{cell} is the electrode surface area of the electrolyzer, and n_d is the electro-osmotic resistance coefficient, I_{ELY} is the working current of the electrolyzer.

The operating voltage of a PEM electrolyzer (U_{ELY}) is composed of the open-circuit voltage (U_{rev}), the activation overpotential (U_{act}), and the ohmic overpotential (U_{ohm}) [36]. The U_{rev} is calculated using the Nernst equation. The U_{act} arises from electrochemical reactions and is influenced by various physicochemical parameters such as the operating temperature of the electrolyzer, catalyst selection, and active sites. The U_{act} can be represented by the Tafel empirical equation. The U_{ohm} is caused by the resistance to proton exchange within the components of the ELY. While the ohmic resistance of multiple components, such as the catalyst layer, diffusion layer, and proton exchange membrane, can be expressed using formulas, typically only the ohmic resistance of the proton exchange membrane is considered [33,37,38]:

$$U_{ELY} = U_{\mathrm{rev}} + U_{\mathrm{act}} + U_{\mathrm{ohm}} \tag{14}$$

$$U_{rev} = U_0 + \frac{RT}{2F}\left[\ln\left(\frac{\alpha_{H_2}\sqrt{\alpha_{O_2}}}{\alpha_{H_2O}}\right)\right] \tag{15}$$

$$U_{act} = \frac{RT}{\alpha_a F}\mathrm{arcsinh}\left(\frac{i}{2i_{0,a}}\right) + \frac{RT}{\alpha_c F}\mathrm{arcsinh}\left(\frac{i}{2i_{0,c}}\right) \tag{16}$$

$$U_{\mathrm{ohm}} = R_{\mathrm{ohm}} I = \frac{t_{me}}{\sigma} I \tag{17}$$

where U_0 represents the open-circuit voltage under standard conditions, R is the gas constant, and α_{H2} and α_{O2} are the activities of H_2 and O_2, respectively. The symbol i denotes the current density of the electrolyzer, while $i_{o,a}$ and $i_{o,c}$ are the exchange current densities measured at the reference temperature. The parameters α_a and α_c are the charge transfer coefficients for the anode and cathode, respectively. The thickness of the proton exchange membrane is denoted by t_{me}, and σ represents the proton conductivity of the membrane, which can be further expressed as a function of the membrane's water content λ and the operating temperature of the electrolyzer T_{ELY} [36]:

$$\sigma = (0.005139\lambda - 0.00326)\exp\left[1268\left(\frac{1}{303} - \frac{1}{T_{ELY}}\right)\right] \tag{18}$$

Fig. 2 presents the model of a 50 Nm^3/h PEM electrolyzer constructed using Simulink. The left segment of the figure delineates the parameter configuration and control mechanisms of the electrolyzer. The central portion of the model, embodying the electrolyzer, is primarily partitioned into four integral components: the cathode model, the anode model, the proton exchange membrane model, and the voltage model. The right segment employs an oscilloscope to exhibit the simulation outcomes of the electrolyzer. This comprehensive model provides a robust framework for understanding and analyzing the performance of PEM electrolyzers.

3.3. Auxiliary system modeling

The auxiliary systems used in the experiment, such as compressors and hydrogen storage tanks, are modeled in the Simulink [36,39,40]:

$$\Delta W_{comp} = \frac{k}{k-1} * F_{H_2}(t) * R * T_{compi} * \left[\left(\frac{P_{compo}}{P_{compi}}\right)^{\frac{k-1}{k}} - 1\right]/\eta_{comp} \tag{19}$$

$$P_{H_2o} = P_{Tanko} + z * \frac{N_{H_2} * R * T_{Tank}}{V_{Tank}} \tag{20}$$

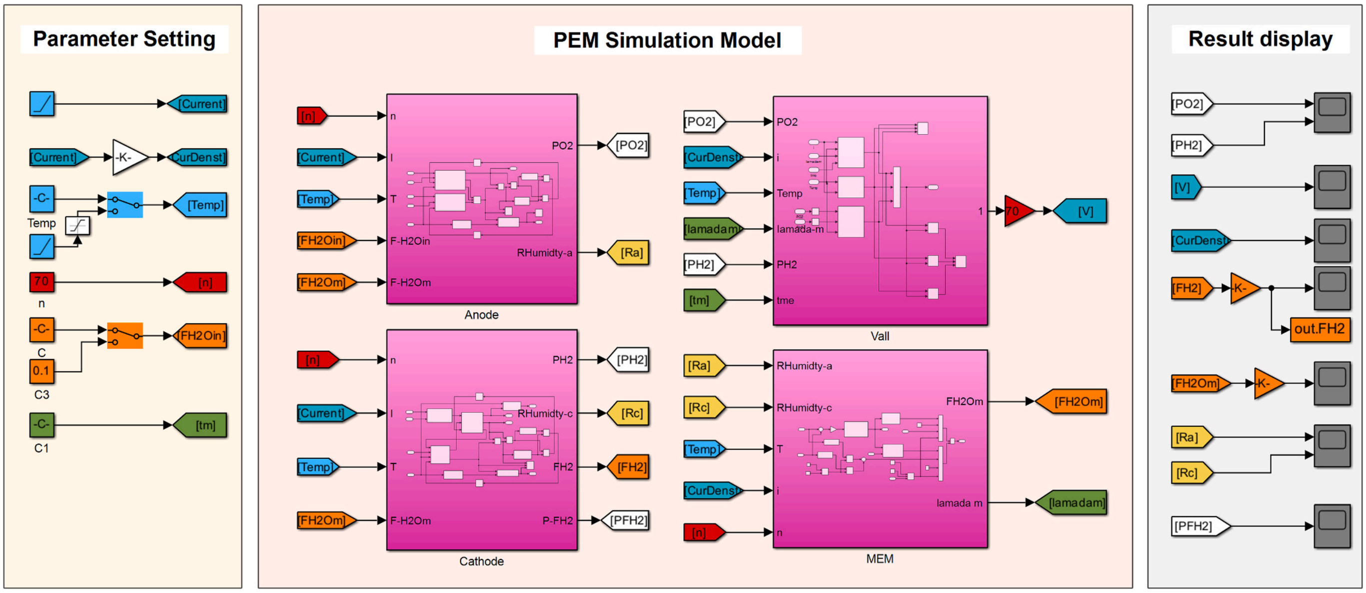

Fig. 2. 50 Nm^3/h PEM electrolyzer model.

$$m_{H_2,\min}^{Tank} \leqslant m_{H_2(t)}^{Tank} = m_{H_2(t-\Delta t)}^{Tank} + F_{H_2}(t) * \Delta t \leqslant m_{H_2,\max}^{Tank} \tag{21}$$

where P_{compi}, P_{compo}, and P_{Tanko} represent the inlet and outlet pressures of the compressor and the hydrogen storage tank, respectively. The z denotes the compressibility factor of hydrogen, while k indicates the hydrogen's polytropic coefficient. T_{compi} represents the inlet temperature of the compressor, and T_{Tank} and V_{Tank} denote the temperature and volume of the hydrogen storage tank, respectively optimal operating conditions. $m_{H_2(t)}^{Tank}$ represents the hydrogen capacity in the storage tank at time (t), $F_{H_2}(t)$ denotes the hydrogen flow rate at time (t), ΔW_{comp} represents the work done by the compressor, and η_{comp} indicates the efficiency of the compressor.

Both the estimation and the validation of the models were performed against experimental data derived from the system operation.

3.4. System evaluation and optimization calculation

The Simulink models used in the direct coupling system experiment conducted in this study have been detailed in the previous sections. During the optimization calculation of the direct coupling system, N_s and N_p are crucial variables in the entire optimization process. Initially, a specific number of N_s and N_p in the PV panels is assumed, and then the hourly solar irradiance data for the entire year is input into the PV system to obtain the current and voltage data generated by the PV system at that moment. If the current data falls within the operating range of the electrolyzer, the current data is input into the hydrogen production system to calculate the gas production at that moment. If the current data is outside the operating range of the electrolyzer, the irradiance and current data for that moment are discarded, and the next moment's irradiance data is read to repeat the above process. After reading the irradiance data for the entire year, the gas production at all moments is summed to obtain the total annual gas production. Based on the fluctuations in the total investment cost over the system's entire life cycle, the highest and lowest LCOH for this number of N_s and N_p in the PV panels are calculated. The life-cycle economic analysis in this study introduces innovative constraints by considering a more detailed range of stages, including procurement and transportation, construction and installation, as well as operation and maintenance of equipment. Unlike previous works, we have expanded the analysis to fully account for the entire cradle-to-grave process of the system, offering a more accurate and comprehensive assessment of the $\mathrm{LCOH_{min}}$ and $\mathrm{LCOH_{max}}$. Finally, the LCOH over the entire life cycle for three routes of distributed PV hydrogen production systems is compared and analyzed [20,41].

$$LCOH = \frac{LCOE + \overline{C}_{CAPEX}^{ETH} + \overline{C}_{OPEX}^{ETH}}{\sum_{\mathrm{i}=1}^{8760} \dot{\mathrm{m}}_{\mathrm{H_2}}^{i}} \tag{22}$$

$$LCOE = \frac{\overline{C}_{CAPEX}^{STE} + \overline{C}_{OPEX}^{STE}}{\sum_{\mathrm{i}=1}^{8760} I_{PV}(\mathrm{t}) * V_{PV}(\mathrm{t})} \tag{23}$$

$$\begin{cases} \overline{C}_{CAPEX}^{ETH} = \left[\sum_{j\in J}\left(\mu_{pur}^{j} N_{ELY}^{j} + \mu_{ins}^{j} Q_{ELY}^{j}\right) + \overline{C}_{CAP}^{comp} + \overline{C}_{CAP}^{Tank}\right] * \dfrac{r}{1-(1+r)^{-n}} \\ \overline{C}_{OPEX}^{ETH} = \overline{C}_{OP\_mat}^{ETH} + \overline{C}_{OP\_main}^{ETH} + \overline{C}_{OP\_lab}^{ETH} + \overline{C}_{OP\_oth}^{ETH} \\ \overline{C}_{CAPEX}^{STE} = \left[\overline{C}_{CAP\_con}^{STE} + \overline{C}_{CAP\_pur}^{STE} + \overline{C}_{CAP\_ins}^{STE} + \overline{C}_{CAP\_land}^{STE}\right] * \dfrac{r}{1-(1+r)^{-n}} \\ \overline{C}_{OPEX}^{STE} = \overline{C}_{OP\_main}^{STE} + \overline{C}_{OP\_lab}^{STE} + \overline{C}_{OP\_oth}^{STE} \end{cases} \tag{24}$$

where *CAPEX* and *OPEX* respectively represent the investment and operating costs. J is the set of electrolyzer types, μ_{buy}^{j} represents the unit purchase price of type j electrolyzers, N_{ELY}^{j} represents the capacity of type j electrolyzers, μ_{ins}^{j} indicates the unit capacity installation cost of type j electrolyzers, and Q_{ELY}^{j} represents the capacity of type j electrolyzers, *con*, *pur*, *ins*, *land*, *mat*, *main*, *lab*, and *oth* the costs associated with construction, purchase, installation, land, raw materials, maintenance, labor, and other expenses, respectively. The symbol r represents the discount rate, and n represents the life cycle duration.

Finally, calculate the system efficiency under the economically optimal conditions based on the high heating value of hydrogen (HHV_{H2}) and the area of PV panels (A_{PV}) at this time [20]:

$$\eta_{STE} = \frac{\sum_{\mathrm{i}=1}^{8760} I_{PV}(\mathrm{t}) * V_{PV}(\mathrm{t}) * 3600}{\sum_{\mathrm{i}=1}^{8760} I_T(\mathrm{t}) * A_{PV}} \tag{25}$$

$$\eta_{STH_2} = \frac{\sum_{\mathrm{i}=1}^{8760} F_{H_2}(\mathrm{h}) * HHV_{H_2}}{\sum_{\mathrm{i}=1}^{8760} I_T(\mathrm{h}) * A_{PV}} \tag{26}$$

The MOPSO algorithm is an enhanced version of the PSO algorithm (Eqs. (27) and (28) [42–44]), which utilizes an external population archive to store all current non-dominated solutions. This archive helps guide the evolutionary direction of the population towards approximating the true Pareto front. In our approach, we modified the objective function used in previous studies. Specifically, we changed the original single-objective LCOH function to a dual-objective formulation, minimizing both $\mathrm{LCOH_{min}}$ and $\mathrm{LCOH_{max}}$ simultaneously to achieve a more comprehensive optimization. This adjustment better reflects the real-world energy flow and market economy changes. When the population exceeds the boundary, the algorithm does not simply assign boundary values, but instead assigns values that respect the system's constraints. To prevent premature convergence and repeated boundary searches, we introduced random perturbations through a mutation operator, which enhances the algorithm's exploration capabilities and robustness.

$$V_{i+1}(t+1) = \varpi * V_i(t) + rand * C_1 * (y_i(t) - x_i(t)) + rand * C_2 * \left(P_g(t) - x_i(t)\right) \tag{27}$$

$$x_i(t+1) = x_i(t) + V_i(t+1) \tag{28}$$

$$X(t+1) = \begin{cases} X(t+1), X_{\min} \leqslant X(t+1) \leqslant X_{\max} \\ X_{rab}(t), X(t+1) < X_{\min} \\ X_{rab}(t), X(t+1) > X_{\max} \end{cases} \tag{29}$$

where *$V_i(t)$*and *$V_{i+1}(t+1)$*are the velocities of searching in the left and right directions for the optimal result in the i^{th} and $(i+1)^{th}$ iterations, respectively, ϖ is the inertia weight, with a larger inertia weight facilitating global search and a smaller inertia weight favoring local search, *rand* is a random number uniformly distributed between 0 and 1. And $y_i(t)$ is the most favorable position of the particle in the preceding iteration, while P_{best} is the globally iterated optimal position of the particle swarm, $x_i(t)$ is the positions of the particle in the i^{th} iterations, C_1 and C_2 are coefficients that represent individual and global learning parameters, respectively.

Fig. 3 illustrates the optimization process flowchart of the MOPSO algorithm in this distributed PV hydrogen production experiment.

4. Results and discussions

After the overall description and modeling of the experimental system, the next step is to validate the accuracy of the model. Subsequently, the optimization algorithm is applied to the distributed system model. Finally, the LCOH obtained from various experimental routes in this study is compared and analyzed, and referenced against the simulation results from other similar studies.

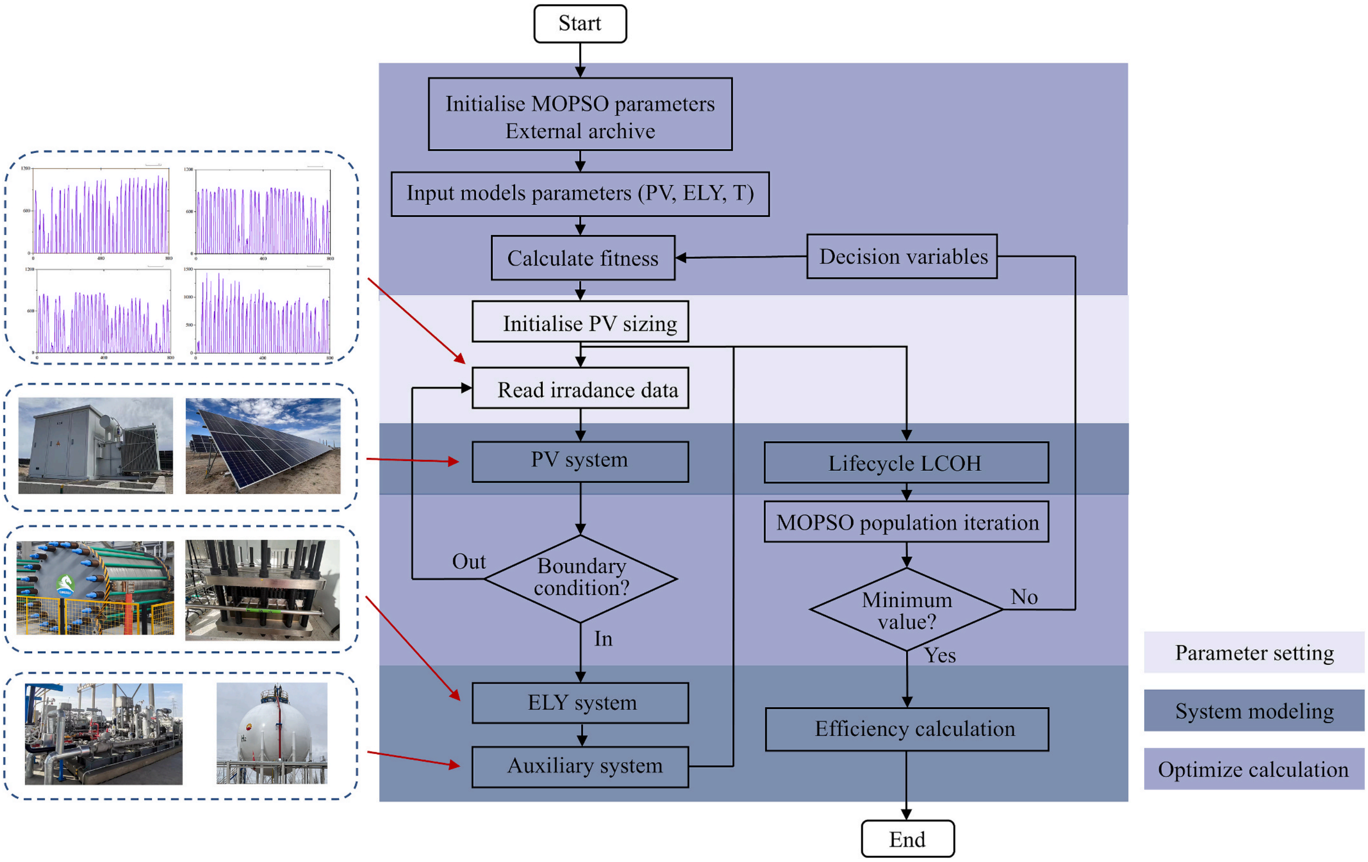

Fig. 3. The flowchart of the optimization process.

4.1. *The impact of external factors*

The impact of external factors includes real-world energy fluctuations such as changes in irradiance and temperature, as well as constraints on grid integration.

Fig. 4 elucidates the influence of irradiance and temperature on the power generation capacity of an individual PV panel. The meteorological data for Yumen City, simulated using Simulink, is sourced from the Xihe Energy Network (https://xihe-energy.com/#climate). For the direct coupling system simulation experiment, one day from each of the four quarters of the year was selected based on actual climatic conditions. The simulation was conducted under two scenarios: maintaining a standard irradiance condition of 1000 W/m^2 while simulating the actual temperature variations of the selected day, and maintaining a standard temperature condition of 25 °C while simulating the actual irradiance variations of the selected day. The main part of the IES, electrolyzers, are located indoors, which minimizes their exposure to environmental factors, even during winter. The results indicate that, compared to temperature conditions, irradiance conditions have a much greater impact on PV panels. When maintaining a constant temperature and simulating actual irradiance variations, the PV current exhibits a highly consistent and rapid hourly variation trend with irradiance. In Q1 and Q4, the current begins to rise between 9:00 and 10:00 and drops to 0A between 19:00 and 20:00. The Q2 and Q3 have significantly better sunlight duration and irradiance conditions compared to the Q1 and Q4, with the current starting to rise between 7:00 and 8:00 and dropping to 0A between 21:00 and 22:00. When maintaining a constant irradiance and simulating actual temperature variations, the maximum and minimum current variations with temperature in the four experiments are 0.47 % and 0.25 %, respectively. Tabbi Wilberforce and Mraoui et al. [5,26] also accounted for the discrepancies between actual and measured meteorological values, as well as individual differences in PV panels, in their experimental and simulation studies. Their research findings suggest that a current fluctuation of merely a few tenths of a percent is entirely acceptable, thereby underscoring the robustness of the system under varying conditions. In light of the aforementioned experimental results, this study will specifically focus on the impact of irradiance on the power generation capacity of PV panels. This approach simplifies the experimental system model, reduces computational complexity, and enhances the efficiency of the research process, thereby demonstrating the robustness of the proposed system under real-world energy fluctuations.

To address the uncertainty associated with irradiance, this study incorporates a full year's worth of high-resolution data (8,760 hourly values), thereby capturing long-term temporal variations and reducing bias due to short-term anomalies. Furthermore, to mitigate the impact of high-frequency noise and enhance the representativeness of the input data, a signal decomposition technique was applied to the irradiance dataset. In this method, variations in the data were separated into low-frequency components (representing broader early trends) and high-frequency components (representing terminal fluctuations). We then reconstructed the time series by replacing the high-frequency components with smoothed low-frequency trends, maintaining the statistical integrity of the data. Fig. 5 illustrates the signal processing methodology applied to stochastic 480-h irradiance data, demonstrating a maximum signal error of 0.88 % over a one-week interval and a cumulative error of 0.49 % across the full 480-h period. This approach effectively limited the annual irradiance input errors to within 1 %, thus ensuring that the solar input data are both representative and robust for simulation purposes.

Both of the indirect coupling methods between the distributed PV station and the IES in our study utilize the independent 35 kV grid of the Yumen Oilfield as the AC bus. This configuration inherently mitigates the limitations imposed by the external grid on the hydrogen production power source. In practical engineering terms, the AC bus does not

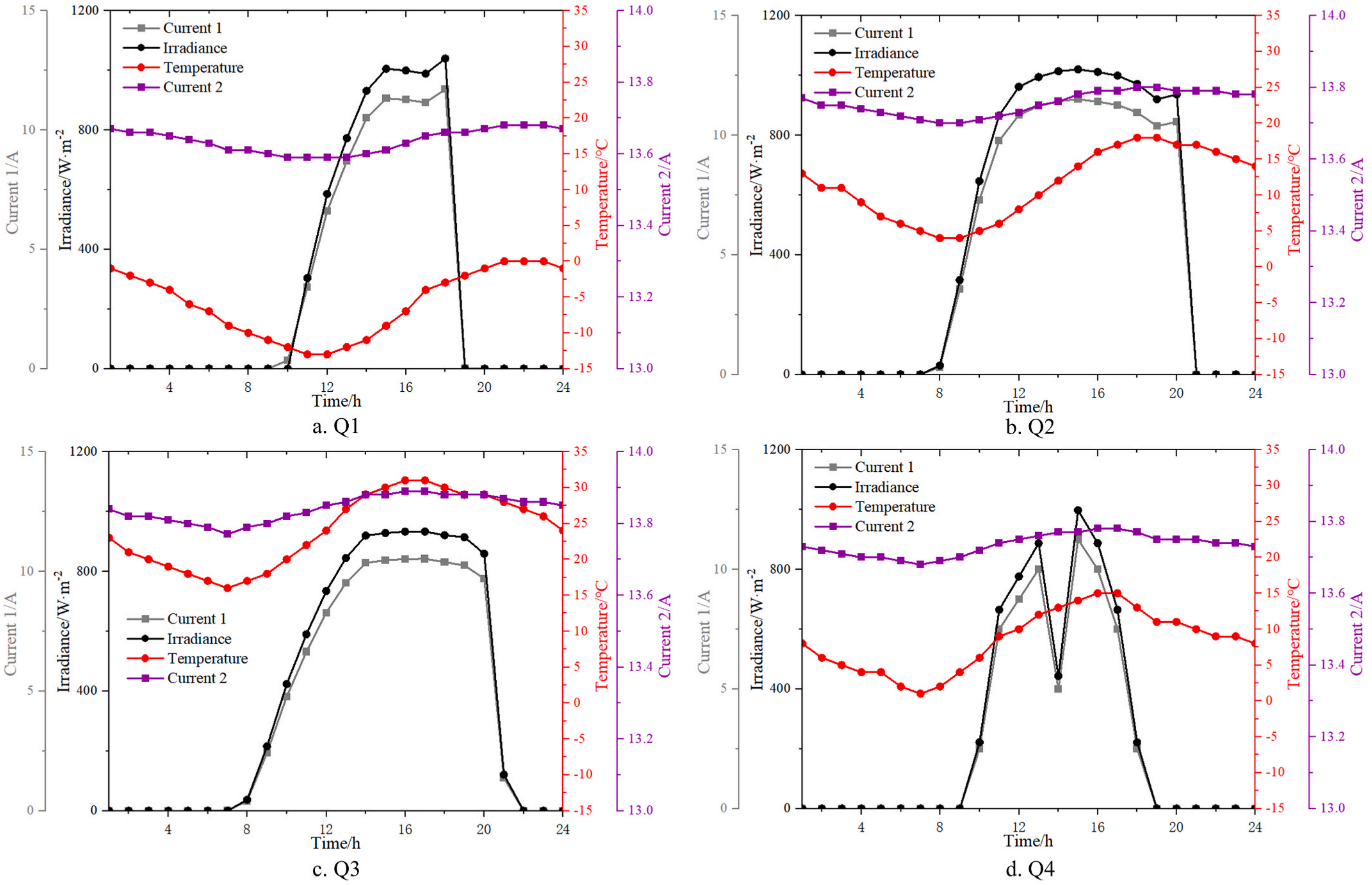

Fig. 4. Comparison of the effects of temperature and irradiance conditions on PV panels in different quarters.

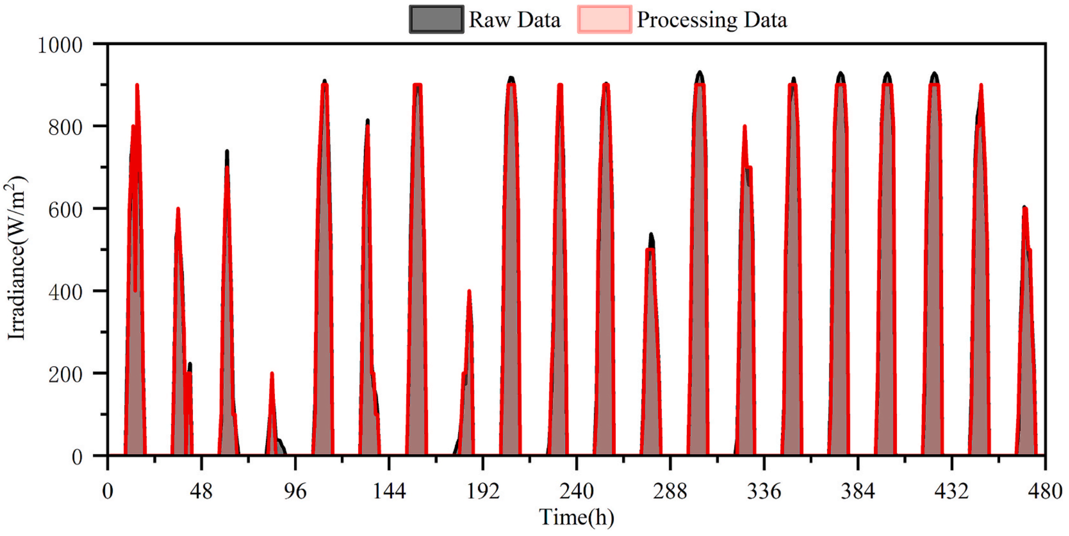

Fig. 5. Signal processing example of random 480 h irradiance data.

necessarily have to be 35 kV; any off-grid hydrogen production technology would involve an AC bus, thus avoiding grid integration constraints. The broader dynamics of the power grid, including the impact of electricity pricing policies on LCOH and transmission restrictions across multiple grid nodes, will be explored in future work.

4.2. Model results validation

In operation, the PEM electrolyzer exhibits a reversible voltage of 1.23 V, a thermal neutral voltage of 1.48 V [42,43], and an optimal operating temperature of 80 °C. The efficiency of voltage hinges on current density and temperature variables. Fig. 6 illustrates the fluctuation in voltage efficiency as per the model adopted in this paper.

This study also conducted a comparative analysis between the

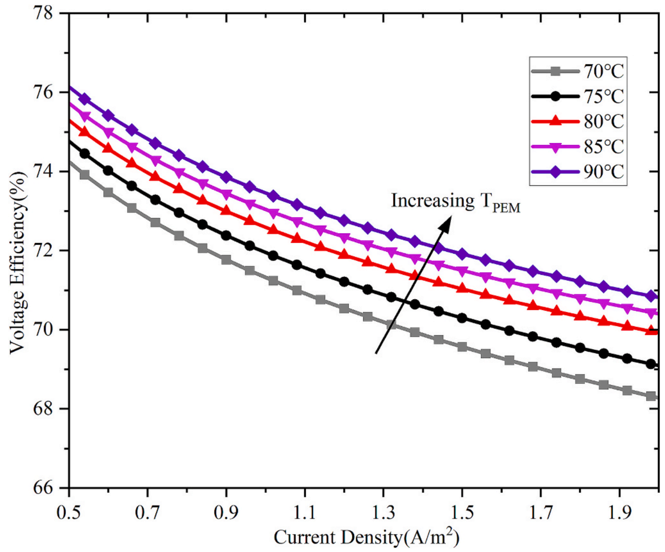

Fig. 6. The voltage efficiency of the PEM electrolyzer varies with current density and temperature.

simulated data derived from the PEM model and the actual data obtained from the applied PEM electrolyzer. This comparison was predicated on the research methodology proposed by Xin et al. [44]. This juxtaposition comparison helps to verify the accuracy of the PEM model and its applicability in real-world scenarios. Fig. 7 presents a comparison between the simulated outcomes of a 50Nm^3/h PEM electrolyzer and the empirical data derived from a 50Nm^3/h PEM electrolyzer employed in practical applications, thereby validating the accuracy of the simulation model. As shown in Fig. 6, the results of the simulation study are fundamentally in alignment with the on-site measurement results. At the inception of the PEM electrolyzer operation, the discrepancy between the two datasets was relatively substantial, reaching 18 %. However, this error rapidly diminished and stabilized below 4 %, with an overall difference rate of 1.36 %. Taking into account the unstable voltage at the beginning of the electrolyzer's operation and the fact that the electrolyzers operate less under low loads, the above results indicate that the dual-stack 200Nm^3/h PEM electrolyzer model, which is constituted by the 50Nm^3/h PEM electrolyzers, exhibits a high degree of accuracy and satisfactorily meets the prerequisites for comparing the direct coupling simulation experiment with the indirect coupling physical experiment.

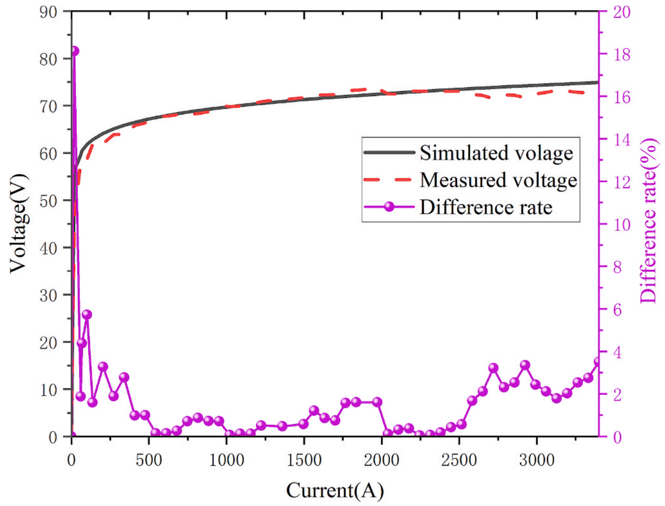

Fig. 7. The difference between the simulated curve and the measured curve of the PEM electrolyzer system.

This study's direct coupling system experiment is designed to couple five 1 MW PV plants with five PEM hydrogen production containers, each with a 200Nm3/h capacity. A single PV plant coupled with a single PEM hydrogen production container can be considered as one direct coupling unit. Within each unit, the PEM electrolyzer has a rated current of 6800A and an operating range of 5 %–120 %, which means the minimum operating current of the electrolyzer is 340A, and the maximum operating current is 8000A. Any current generated by the PV system that exceeds this operational range is consequently discarded. In the application of the MOPSO algorithm for computational optimization tasks, the initial population size is configured to be 40, and the dimensionality of the search space is configured to be 4. This configuration implies that the optimization process is conducted with two particles, each operating in its own 4 dimensions. Subsequent to the adjustment of parameters, the learning factors, C_1 and C_2, are established at 1.4962, and the inertia weight, the Greek letter ω, is determined to be 0.7298. These specific parameter settings are strategically chosen to strike a balance between minimizing the number of iterations and preserving the precision of the solution. This approach ensures an efficient and accurate optimization process.

This study selects metaheuristic algorithms instead of mathematically-based approaches because metaheuristic algorithms can sacrifice a certain degree of accuracy in exchange for improved solution efficiency [45]. In this field, such accuracy loss is considered completely acceptable [22].

In metaheuristic algorithms, MOPSO extends the classical particle swarm optimization (PSO) algorithm by incorporating the Pareto principle to handle multi-objective problems (originally proposed by Kennedy and Eberhart [46] in 1995 and improved by Shi and Eberhart [47] in 1999 with inertia weighting). Compared to algorithms like NSGA-II, MOPSO can effectively navigate complex search spaces through inertia weights [48], avoid premature convergence [48], and handle complex problems efficiently through parallel particle evaluation (such as our 8760h dataset). Additionally, MOPSO preserves feasible solutions by establishing external archives [49] (e.g., current ≤8000 A).

To balance the feasibility of the algorithm with practical engineering requirements, this article has defined the current experimental scale. If faced with large-scale optimization problems in the future, our algorithm (MOPSO) can be directly extended to such scenarios [50], either by increasing the number of particles and iterations or by integrating more advanced strategies, such as surrogate models or distributed computing, to improve computational efficiency. While our current implementation focuses on smaller-scale cases, we acknowledge that future research will explore the scalability and performance of MOPSO in more complex, large-scale environments.

Fig. 8 illustrates the comparison of Pareto fronts obtained from MOPSO and NSGA-II in the directly coupling experiment (a) and analysis of LCOH convergence in the MOPSO algorithm optimization process (b).

The results indicate that the Pareto front generated by MOPSO is closer to the true front in the solution space (f_1: $LCOH_{min}$, f_2: $LCOH_{max}$) compared to NSGA-II, demonstrating its superior convergence in solving the PV-IES coupling problem. For the optimization of f_1, MOPSO converged the $LCOH_{min}$ to € 2.93/kg, whereas NSGA-II achieved € 3.07/kg, representing a reduction of 4.78 %. For the optimization of f_2, MOPSO converged the $LCOH_{max}$ in extreme scenarios to below € 2.99/kg, while NSGA-II resulted in € 3.12/kg, achieving a reduction of 4.35 %. Fig. 8 (b) illustrates the rapid global exploration (iterations 1–50) and local refinement (iterations 51–150) of MOPSO, which eventually stabilized between € 2.93–2.99/kg.

Table 3 lists the MOPSO simulation optimization solution for directly coupled systems, including investment cost, annual hydrogen production, abandonment rate, and LCOH range for different sizes of PV panels within each unit in the simulation experiment. The MOPSO algorithm maintains the Pareto front, which preserves the equilibrium solutions of different objectives in the "optimal" solution set rather than a single

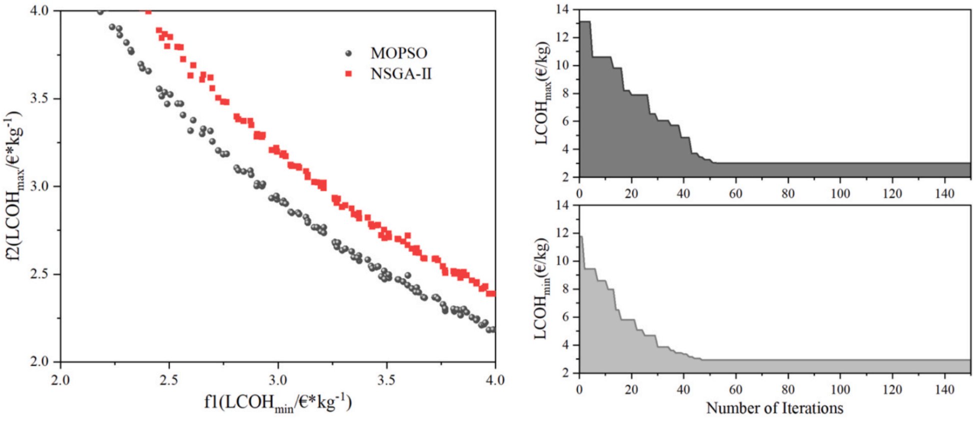

a. Comparison of Pareto frontiers obtained from MOPSO and NSGA-II in the direct coupling experiment

b. Analysis of LCOH Convergence in MOPSO Algorithm Optimization Process

Fig. 8. Optimization Performance and Convergence Analysis of MOPSO Algorithm.

Table 3
MOPSO simulation optimization solution for the direct coupling system.

	$N_p = 3$ $N_s = 377$	$N_p = 3$ $N_s = 500$	$N_p = 3$ $N_s = 600$	$N_p = 3$ $N_s = 613$	$N_p = 3$ $N_s = 650$
Investment cost (€ 1 × 10^6)	7.41–7.67	7.88–8.14	8.2–8.46	8.33–8.59	8.23–8.37
m_{H2} (1 × 10^3 Nm^3)	1801.5	2371.5	2754.5	2766.5	2720.5
Abandonment rate (%)	0	0.15	0.99	2.90	6.92
LCOH (€/kg)	4.09–4.24	3.29–3.41	2.97–3.05	2.93–2.99	2.99–3.07

optimal solution. This method avoids the solution set being too concentrated in a certain part and also avoids getting stuck in local optima.

In direct coupling systems, optimizing the PV-ELY system configuration is essential to maximize STH efficiency or minimize the LCOH. To achieve this, the I-V curve of the ELY should closely align with the Maximum Power Point Line (MPL) of the PV system. This alignment can be obtained by adjusting the number of ELY cells and PV panels connected in series or parallel (N_s, N_p). In directly coupled PV-ELY systems, optimization efforts primarily focus on modifying the number of connected PV panels and ELY cells to maximize energy transfer efficiency, STH efficiency, and hydrogen production while minimizing energy losses [22]. After considering both hydrogen production and light abandonment rate in the "optimal" solution set obtained by MOPSO, Ns = 613 and Np = 3 were ultimately chosen as the final solutions for each unit. At this point, the total investment cost is € 8.33–8.59 × 106. Under this condition, the annual hydrogen production is 2.77 × 106 Nm^3, equivalent to 246.2 tons, with an abandonment rate of 2.9 %. Under these parameters, the final LCOH range reaches € 2.93–2.99/kg. At this point, the scale of the PV panels within each unit is 540.2 W*3*613 = 0.993 MW, approximately 1 MW.

4.3. Comparison of experimental results

The financial evaluation described in this paper is based on an exchange rate that stipulates one unit of RMB is equivalent to 0.13 units of EUR. This exchange rate is a fundamental parameter for all economic analyses conducted within the scope of this study. Table 4 presents the life cycle investment cost estimate for a 5 MW distributed PV hydrogen production system, including costs for construction, purchase, installation, land, raw materials, maintenance, labor, and other expenses. The PV, hydrogen production, and auxiliary systems all use the straight-line depreciation route, with a system lifespan of 20 years. The PV panels depreciate at 5 % per year, while the electrolyzers, compressors, and hydrogen storage tanks depreciate at 3 % per year. The cost of PV mounting brackets is € 1105/t, and every electrolyzer consumes 2 tons of raw water and cooling water annually. The cost of the PEM electrolyzer is considered the overall cost of the container, while the ALK electrolyzer requires separate calculations for the gas–liquid separation and TSA purification equipment costs. Based on the actual construction situation of the Yumen Oilfield hydrogen production project, the discount rate is set at 8 %, and the investment payback period is 11.56 years. The specific economic parameters at each stage of the life cycle are detailed in Table 4, and the range of economic parameters, to some extent, reflects market fluctuations.

Table 4
Life cycle investment cost estimate.

	Construction (€ 1 × 10^3)	Purchase	Installation	Land	Materials	Maintenance and labor	Other (€ 1 × 10^3)
PV	104–130	€ 0.22/W	€ 2.6/kW	€ 0.35/m^2	/	7 %	234–250
Energy Storage	65–104	€ 130–169 × 10^3	€ 11–13 × 10^3		/	5 %	
PEM	/	€ 3900/Nm^3	€ 260 × 10^3		€ 0.6552/t	5 %	/
ALK	/	€ 1040/Nm^3	€ 52 × 10^3	/		5 %	689–750
Comp	/	€ 39–52 × 10^3	€ 3–6 × 10^3	/	/	3 %	/
Tank	/	€ 208–234 × 10^3	€ 17–20 × 10^3	/	/	3 %	/

Fig. 9 presents a longitudinal comparative analysis of several academic articles [18,23,51–54]. Each article discusses the efficiency of PV panels, electrolyzers, and the entire direct system. In the early stages of direct coupling system research, monocrystalline silicon was the preferred material for manufacturing PV panels. As the field developed, materials such as polycrystalline silicon began to emerge. In a 2019 study conducted by Tuyen Nguyen Duc et al. [51], the heterojunction intrinsic thin layer material was employed. A similar trend can be observed in the choice of electrolyzers for direct coupling systems. ALK electrolyzers were primarily used in early experiments, but due to their poor adaptability to fluctuating power sources, current research on direct coupling systems predominantly employs PEM electrolyzers [22,55]. In 2016, Farid Sayedin et al. [18] conducted a study using meteorological data from different regions of Iran, which showed that the PV efficiency in various regions of Iran was 14 %, and the efficiency of PEM electrolyzers ranged from 68 % to 75 %. Subsequently, a 20 kW experimental study conducted in Japan in 2019 demonstrated an increase in PV efficiency to 17.2 % and a surge in PEM efficiency to 86.5 %, resulting in an overall system efficiency of 14.9 % [51]. In this paper, the obtained PV efficiency was 23.55 %, PEM efficiency was 74.88 %, and the overall system efficiency increased to 17.64 %. The decrease in PEM efficiency in this study compared to the 2019 study in Japan can be attributed to optimization calculations aimed at minimizing LCOH [51], where the PEM electrolyzers operated at low load for part of the time, preventing the full realization of the PEM electrolyzers' maximum potential. If the experimental system in this study were optimized with the goal of maximizing system efficiency, a more significant efficiency value could be achieved.

Fig. 10 presents a longitudinal comparison between the direct coupling experiment in this study and two of the most representative economic studies to date. The first study, conducted by Farid Sayedin et al. in 2016, utilized meteorological data from various regions of Iran [18]. At that time, the cost of PV panels was € 4/W, with operating costs at 2 % of the investment cost, and PEM electrolyzers priced at € 1/W with an annual depreciation rate of 15 %. The resulting LCOH across different regions of Iran ranged from € 7.32–9.46/kg. Subsequently, a 2019 study by Diederik Coppitters et al. [51], which used meteorological data from multiple locations worldwide, indicated that the cost of PV panels had decreased to approximately € 0.78/W, which is 19.5 % of the cost reported in the Iranian study three years earlier. The cost of PEM electrolyzers also dropped to € 1.75/W, with a depreciation rate of 6 %. Johannesburg emerged as the most advantageous city among several, with an LCOH ranging from € 6.3–6.9/kg. In the present study, the cost of PV panels has further decreased to € 0.22/W, and the cost of PEM electrolyzers has dropped to € 1.03/W. The LCOH obtained from the life cycle assessment in this study ranges from € 2.93–2.99/kg.

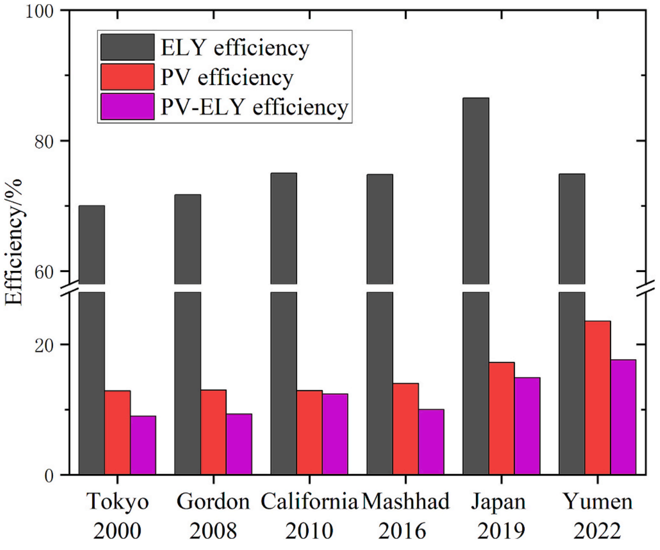

Fig. 9. Comparison of direct coupling system efficiency.

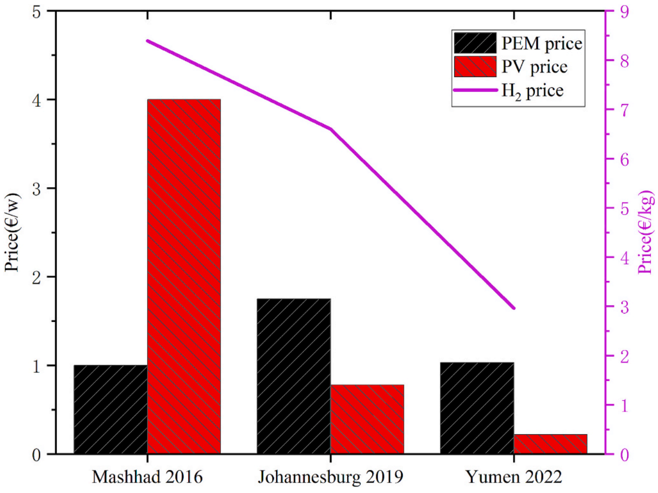

Fig. 10. Comparison of direct coupling system economic performance.

Table 5 further compares the optimization techniques, performance indicators, and research results of all PV-ELY hydrogen production systems mentioned in Figs. 9 and 10 above. In these studies on direct coupling systems, there is a common research principle, which is to optimize the I-V curves of PV panels and electrolytic cells by correctly selecting their N_s and N_p, so that the system operates near the maximum power point (MPP), thereby achieving efficient energy transfer. Compared with these studies, the direct coupling optimization experiment in this study adopts the same research principle, similar research platforms, more advanced optimization algorithms, and different optimization objectives, so the research results are connected and comparable. A large number of simulation studies and some experimental studies have proven the rationality and feasibility of this method.

The economic indicators of the three coupling routes for distributed PV hydrogen production are detailed in Table 6. The investment cost of PEM direct coupling systems using DC is slightly lower than that of indirect coupling systems using AC. For a distributed scale of 5 MW, direct coupling PEM systems can save approximately 3 % of the total investment cost. Moreover, using DC coupling can significantly improve the utilization rate of PEM electrolyzers, with the annual equivalent utilization hours and annual hydrogen production being 1.49 times that of using AC. When using AC coupling, a series of power electronic components and energy storage devices are required. In this indirect coupling study, the comprehensive reduction factor during the experiment was approximately 87 %. A 5 MW PV power station can generate 11,589 MWh annually, with the PV panels having an annual equivalent utilization of 1759.5 h.

Fig. 11 shows the cost output proportions of the three coupling routes. The expenditure differences for PV power stations among the three distributed hydrogen production routes are not significant, with direct coupling being slightly lower than indirect coupling. Regardless of the coupling route, if PEM electrolyzers are used, the cost of the integrated hydrogen production plant will account for more than 70 % of the total cost expenditure. In this case, the DC direct coupling route can improve the utilization rate of PEM electrolyzers and increase annual hydrogen production, thereby partially offsetting the LCOH. However, the resulting LCOH is still higher than that of the AC indirect coupling with ALK electrolyzers. This is due to the lower procurement cost of ALK electrolyzers, which can significantly reduce the total investment cost of distributed PV hydrogen production systems. Among the three distributed hydrogen production routes, DC direct coupling with PEM electrolyzers results in the highest annual hydrogen production, while AC

Table 5
Comparative analysis of optimization techniques and performance metrics in PV-ELY systems for hydrogen production [22].

Ref	Objectives	Technique	Contributions & results	Platform
This study (2024)	Minimise $LCOH_{min}$, Minimise $LCOH_{max}$,	MOPSO	Comprehensively analyzed both direct and indirect coupling of PV and electrolysis systems, providing new insights into the cost-effectiveness and long-term potential of solar-driven hydrogen production. For the direct coupling of PV power generation with PEM, Simulink is used for experiments. For indirect coupling, experimental data from distributed PV power stations and PEM and ALK in practical application at the Yumen Oilfield are used.	MATLAB
Coppitters et al. [20] (2019)	Minimise LCOH	NSGA-IISRDO	Proposed both deterministic and robust designs and a global sensitivity analysis on the hydrogen production and LCOH of the direct coupled PV-ELY system under techno-economic uncertainty. The optimal system gives a minimum LCOH between € 6.3/kg and € 10.5/kg.	–
NGUYEN DUC T et al. [51] (2019)	Minimise energy losses	GA and Test	Presented a high-efficiency, large-scale (20 kW-class) direct-coupled PV-PEM electrolyzer system for hydrogen production. Furthermore, a genetic algorithm (GA)-based simulation model was developed using on-site operational data. validated the system's scalability, environmental benefits, and applicability for future industrial deployments.	LabView
Sayedin et al. [18] (2016)	Minimise energy losses, Minimise LCOH	PSO	Proposed a size optimisation approach that considers climate conditions' impacts and two optimisation objectives. Technical and economic criteria have been included to optimise the system design. Six case studies with different weather and solar irradiation conditions are carried out to compare the results geographically.	MATLAB
GIBSON T L et al. [54] (2010)	Maximise STH efficiency	Test-and-select	Proposed a comprehensive model for PV-ELY efficiency prediction, with 0.4 % accuracy. The H_2 production efficiency of 12.4 % was achieved.	Excel
GIBSON T L et al. [53] (2008)	Maximise STH efficiency	Test-and-select	Described a compact size and simplicity of an optimised direct coupled PV-ELY system, which could supply both home fuel cell electric vehicle (FCEV) refuelling and a home power generation system. The STH efficiency of 12.4 % was achieved.	Excel
TANI T et al. [23] (2000)	Minimise energy losses	Test-and-select	Proposed an H_2 cost function to optimise the PV-ELY system. In addition, the study presented a comparison of the experimental and modelling results.	

Table 6
Economic comparison of three coupling routes.

	Total cost (€ 1 × 10^6)	Equivalent utilization hours of electrolyzers(h)	m_{H2} (1 × 10^3 Nm^3)	LCOH(€/kg)	
				Min	Max
Direct + PEM	8.33–8.59	2750	2766	2.93	2.99
Indirect + PEM	8.49–8.86	1847.9	1848	4.47	4.65
Indirect + ALK	4.36–4.61	1655.8	1656	2.55	2.68

indirect coupling with ALK electrolyzers achieves the lowest LCOH.

4.4. Parameters sensitivity analysis

The life cycle of hydrogen production by coupling distributed PV power stations with IES can be broadly divided into three stages: the land acquisition, leasing, and construction stage (LCS); the equipment purchase and installation stage (PIS); and the operation and maintenance stage (OMS) during the normal functioning of the distributed PV hydrogen production station. The sensitivity parameters within these three stages are denoted as Land & Con, Pur & Ins, and Oper & Main, respectively. These factors are analyzed across three coupling routes to explore the impact mechanisms of distributed PV hydrogen production [40]. The sensitivity parameters are varied within the range of [−20 %, 20 %]. The sensitivity analysis results for each stage's impact on the LCOH are shown in Fig. 12.

Sensitivity analysis reveals that the three sensitivity parameters, Land & Con, Pur & Ins, and Oper & Main, are all positively correlated with the LCOH. The LCS, as well as the OMS, has similar impacts on the LCOH over the whole life cycle. For the direct coupling of PEM IES, the impact of the LCS is greater than that of the OMS during normal operation. In contrast, for the other two routes, the impact of the OMS is slightly greater than that of the LCS. This is because the direct coupling route eliminates a significant amount of power electronic equipment, thereby saving on the permanent land acquisition, leasing, and construction costs of the PV station. Additionally, the operation and maintenance costs of ALK IES are significantly lower than those of PEM IES. For all three coupling technology routes, the PIS has the greatest impact on the LCOH. Furthermore, the indirect coupling of PEM IES involves the most equipment and the most complex route, thus having the greatest impact on the LCOH.

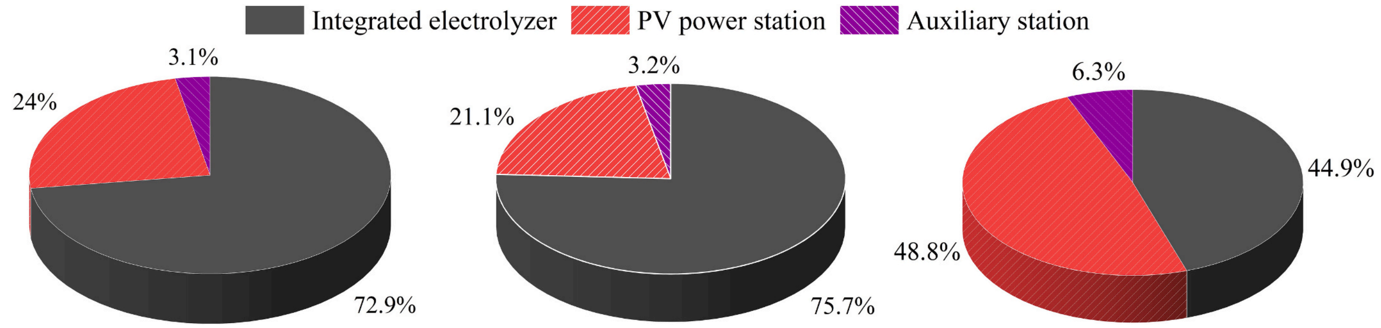

Fig. 11. The cost output proportions of the three coupling routes.

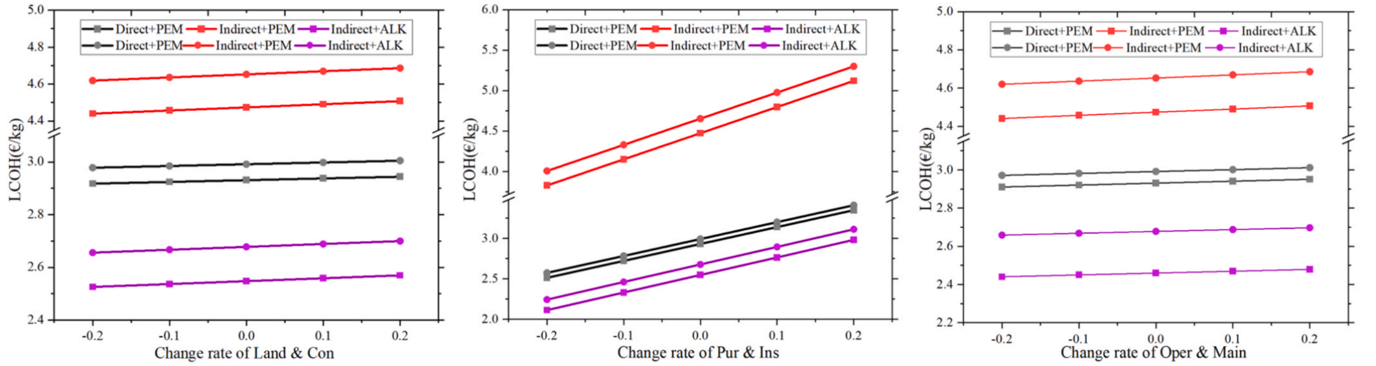

a. Sensitivity analysis of Land & Con to LCOH b. Sensitivity analysis of Pur & Ins to LCOH c. Sensitivity analysis of Oper & Main to LCOH

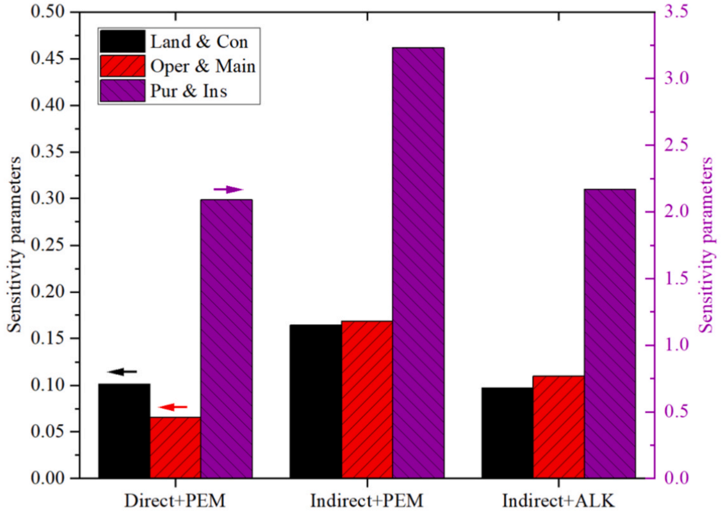

d. Comparison of sensitivity parameters in three stages

Fig. 12. Comparison of sensitivity to LCOH in three stages of the whole life cycle.

To comprehensively investigate the system’s sensitivity characteristics, we conducted an in-depth sensitivity analysis focusing on the procurement and installation phases of both the PV power station and the IES. The analytical results are presented in Fig. 13.

Fig. 13(a) shows how the LCOH changes with the variation in the change rate of the distributed PV station. The chart illustrates that as the change rate of the PV station increases (either positively or negatively), the LCOH tends to increase. The indirect coupling route exhibits higher sensitivity to the distributed PV station. Fig. 13(b) presents the sensitivity of the LCOH with respect to the change rate of the IES. The sensitivity of PEM IES is higher, and for Indirect + ALK, the sensitivity of distributed photovoltaic power plants and IES is similar. Fig. 13(c) indicates that the Indirect + PEM route shows the most significant sensitivity, particularly in the IES category, while the “Direct + PEM” route exhibits the least sensitivity for both PV stations and IES.

5. Conclusions

This paper conducts a comparative economic analysis of three distributed PV power generation coupled IES routes from a life cycle perspective, emphasizing their feasibility in solar energy applications. The originality of this study lies in the integration of both system modeling and real-world empirical data, providing a comprehensive analysis of the economic performance of these coupling routes in practical settings. The direct coupling experiment involved modeling the system using Simulink, followed by optimization calculations using the MOPSO algorithm to obtain experimental data. The indirect coupling experiment utilized experimental data from a distributed PV power

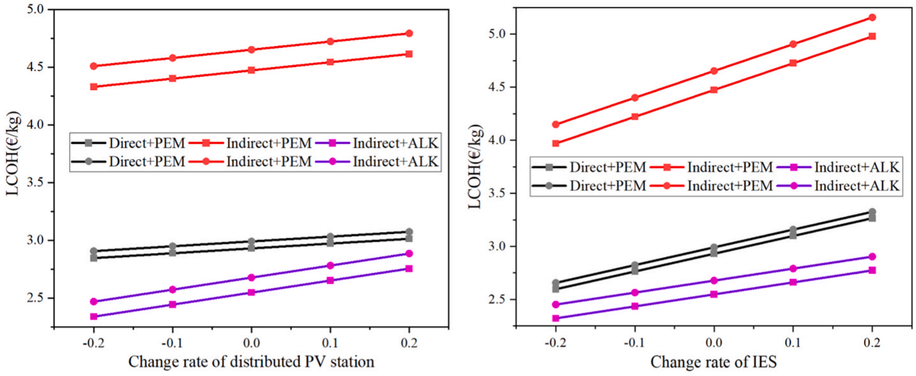

a. Sensitivity analysis of distributed PV station
b. Sensitivity analysis of IES

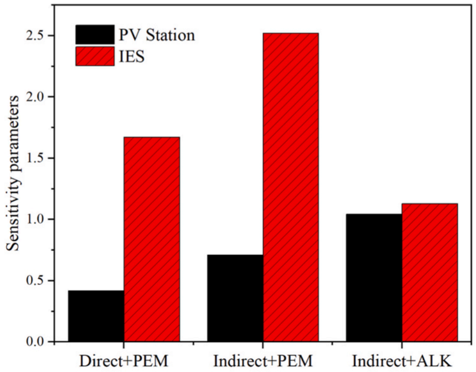

c. Comparison of sensitivity parameters in three routes

Fig. 13. Comparison of sensitivity to LCOH in three stages of the whole life cycle.

station and various ELY in practical applications at the Yumen Oilfield. Through empirical analysis, the following key conclusions were drawn:

1. Advances in Direct Coupling of PV-PEM: In recent years, continuous advancements in solar energy research have significantly improved the system efficiency of PV power generation directly coupled with PEM. The study demonstrates that the LCOH has notably decreased, making this coupling route increasingly competitive. This contribution is significant as it highlights the potential of the direct coupling route in reducing hydrogen production costs, an area with limited research until now.
2. Effectiveness of Direct Coupling in Enhancing Hydrogen Production: While the direct coupling route is generally more suitable for PEM, it effectively maximizes the annual hydrogen production by utilizing the full potential of solar energy. This finding is important for the practical implementation of large-scale solar hydrogen systems, providing valuable insights for energy planners looking to optimize energy yield from renewable sources.
3. Economic Efficiency of Indirect Coupling with ALK IES: The study finds that indirect coupling of distributed PV power stations with ALK IES currently represents the most economically efficient hydrogen production route. In comparison, direct coupling of PEM IES is slightly less economical but remains competitive for specific applications. Indirect coupling of PEM IES still shows a significant economic gap.

The findings of this study have important practical implications for the deployment of distributed solar hydrogen production systems. By comparing the economic viability of different coupling routes, the study provides critical insights for decision-makers in the energy sector. The results can guide the selection of the most cost-effective coupling method based on the specific needs and resources of a region. In particular, the optimization of PV-PEM systems and the consideration of indirect coupling routes could help lower hydrogen production costs, contributing to the advancement of clean hydrogen technologies in real-world applications. This research can inform policy development, funding strategies, and industry investments aimed at scaling up renewable hydrogen production to meet future energy demands.

CRediT authorship contribution statement

Zunbo Wang: Software, Resources, Methodology, Formal analysis, Data curation, Conceptualization. **Yong He:** Visualization, Validation, Methodology, Conceptualization. **Wanzhen Wang:** Resources, Project administration, Methodology. **Zhongtao Liao:** Resources, Methodology. **Wubin Weng:** Visualization, Validation. **Zhihua Wang:** Writing – review & editing, Funding acquisition. **Shengtao Qian:** Writing – review & editing.

Declaration of competing interest

The authors declare that they have no known competing financial interests or personal relationships that could have appeared to influence the work reported in this paper.

Acknowledgments

This work was supported by the Smart Grid-National Science and Technology Major Project (2024ZD0801704), the National Natural Science Foundation of China (52125605), and the Fundamental Research Funds for the Central Universities (2022ZFJH04).

The authors of this article want to express their gratitude to the individuals from the PetroChina Yumen Oilfield for their support during the article's drafting phase.

Appendix A. Supplementary data

Supplementary data to this article can be found online at https://doi.

org/10.1016/j.solener.2025.113747.

References

[1] R. Yasmeen, B. Wang, W.U.H. Shah, et al., Adequacy of photovoltaic power on provincial and regional levels of income inequality in China, Sol. Energy 262 (2023) 111906.

[2] D. Boruah, S. Singh Chandel, A comprehensive analysis of eight rooftop grid-connected solar photovoltaic power plants with battery energy storage for enhanced energy security and grid resiliency, Sol. Energy 266 (2023) 112154.

[3] S.M.G. Dumlao, S. Ogata, Japan's local consumption of solar energy: the role of energy demand in residential and small-scale solar projects, Sol. Energy 287 (2025) 113175.

[4] R. Li, X. Jin, P. Yang, et al., Techno-economic analysis of a wind-photovoltaic-electrolysis-battery hybrid energy system for power and hydrogen generation, Energ. Conver. Manage. 281 (2023) 116854.

[5] H. Miao, Y. Yu, Y. Wan, et al., Levelized cost of long-distance large-scale transportation of hydrogen in China, Energy 310 (2024) 133201.

[6] J. Park, S. Kang, S. Kim, et al., Optimizing green hydrogen systems: balancing economic viability and reliability in the face of supply-demand volatility, Appl. Energy 368 (2024) 123492.

[7] J. Antonanzas, N. Osorio, R. Escobar, et al., Review of photovoltaic power forecasting, Sol. Energy 136 (2016) 78–111.

[8] S.E. Haupt, S. Dettling, J.K. Williams, et al., Blending distributed photovoltaic and demand load forecasts, Sol. Energy 157 (2017) 542–551.

[9] P. Benalcazar, A. Komorowska, Techno-economic analysis and uncertainty assessment of green hydrogen production in future exporting countries, Renew. Sustain. Energy Rev. 199 (2024) 114512.

[10] M.A. Abdelkareem, A.A. Abdelghafar, M. Mahmoud, et al., Optimized solar photovoltaic-powered green hydrogen: current status, recent advancements, and barriers, Sol. Energy 265 (2023) 112072.

[11] Z. Kang, F. Duan, A flexible load adaptive control strategy for efficient photovoltaic hydrogen generation system, Sol. Energy 266 (2023) 112150.

[12] A. Atiz, M. Karakilçik, Assessment of hydrogen generation and thermodynamic efficiencies of PEM coupled with PV and PV-T under diverse circumstances, Int. J. Hydrogen Energy 75 (2024) 132–143.

[13] Y. Fu, Z. Wang, X. Li, et al., Numerical research on building energy balance and grid stability realization of PV/T-ASHP system through electrical-hydrogen coupled storage technology, Energy 307 (2024) 132676.

[14] R. Mas, A. Berastain, A. Antoniou, et al., Genetic algorithms-based size optimization of directly and indirectly coupled photovoltaic-electrolyzer systems, Energ. Conver. Manage. 270 (2022) 116213.

[15] R. Mas, D. Pichilingue, A. Berastain, et al., On the application of sliding mode control to indirectly coupled photovoltaic-electrolyzer systems used in the production of clean energy, Int. J. Thermofluids 23 (2024) 100747.

[16] J. Zhang, Z. Wang, Y. He, et al., Comparison of onshore/offshore wind power hydrogen production through water electrolysis by life cycle assessment, Sustain. Energy Technol. Assess. 60 (2023) 103515.

[17] L. Bentoumi, A. Miles, Z. Korei, Green hydrogen production by integrating a solar power plant with a combined cycle in the desert climate of Algeria, Sol. Energy 268 (2024) 112311.

[18] F. Sayedin, A. Maroufmashat, S. Sattari, et al., Optimization of photovoltaic electrolyzer hybrid systems; taking into account the effect of climate conditions, Energ. Conver. Manage. 118 (2016) 438–449.

[19] M. Zhu, D. Xiang, H. Cao, et al., Techno-economic analysis of green hydrogen production using a 100 MW photovoltaic power generation system for five cities in North and Northwest China, Sol. Energy 269 (2024) 112312.

[20] D. Coppitters, W. de Paepe, F. Contino, Surrogate-assisted robust design optimization and global sensitivity analysis of a directly coupled photovoltaic-electrolyzer system under techno-economic uncertainty, Appl. Energy 248 (2019) 310–320.

[21] K.M. Nguyen, L.V. Phan, D.D. Nguyen, et al., A comprehensive technical analysis on optimal sizing and operating strategy for large-scale direct coupled PV–electrolyser systems, considering PV system faults, degradation and partial shading conditions, Int. J. Hydrogen Energy 59 (2024) 492–506.

[22] L. Phan Van, L. Hieu Hoang, T. Duc Nguyen, A comprehensive review of direct coupled photovoltaic-electrolyser system: sizing techniques, operating strategies, research progress, current challenges, and future recommendations, Int. J. Hydrogen Energy 48 (65) (2023) 25231–25249.

[23] T. Tani, N. Sekiguchi, M. Sakai, et al., Optimization of solar hydrogen systems based on hydrogen production cost, Sol. Energy 68 (2) (2000) 143–149.

[24] U.K. Nkalo, O.O. Inya, O.P. Ifeanyi, et al., A modified multi-objective particle swarm optimization (M-MOPSO) for optimal sizing of a solar–wind–battery hybrid renewable energy system, Sol. Compass 12 (2024) 100082.

[25] Y. Tang, W. Long, Y. Wang, et al., Multi-objective optimization of methanol reforming reactor performance based on response surface methodology and multi-objective particle swarm optimization coupling algorithm for on-line hydrogen production, Energ. Conver. Manage. 307 (2024) 118377.

[26] S. De, P. Rakshit, A.B. Chowdhury, Optimization of time based fuzzy multi-objective reliability redundancy allocation problem for xj−out−of−m system using tuning and neighborhood based fuzzy MOPSO algorithm, Appl. Soft Comput. 149 (2023) 110998.

[27] R. Sellami, F. Sher, R. Neji, An improved MOPSO algorithm for optimal sizing & placement of distributed generation: a case study of the Tunisian offshore distribution network (ASHTART), Energy Rep. 8 (2022) 6960–6975.

[28] A. González Del Valle, P. García-Linares, A. Martí, Optimizing hydrogen production: a comparative study of direct and indirect coupling between photovoltaics and electrolyzer, Energ. Conver. Manage. 315 (2024) 118751.

[29] V.A. Martinez Lopez, H. Ziar, J.W. Haverkort, et al., Dynamic operation of water electrolyzers: a review for applications in photovoltaic systems integration, Renew. Sustain. Energy Rev. 182 (2023) 113407.

[30] J. Wang, J. Wen, J. Wang, et al., Water electrolyzer operation scheduling for green hydrogen production: a review, Renew. Sustain. Energy Rev. 203 (2024) 114779.

[31] T. Yigit, O.F. Selamet, Mathematical modeling and dynamic Simulink simulation of high-pressure PEM electrolyzer system, Int. J. Hydrogen Energy 41 (32) (2016) 13901–13914.

[32] D. Brezak, A. Kovač, M. Firak, MATLAB/Simulink simulation of low-pressure PEM electrolyzer stack, Int. J. Hydrogen Energy 48 (16) (2023) 6158–6173.

[33] S. Sharifian, N.A. Kolur, M. Harasek, Transient simulation and modeling of photovoltaic-PEM water electrolysis, Energy Sour. Part A (2019).

[34] F. Marangio, M. Santarelli, M. Cali, Theoretical model and experimental analysis of a high pressure PEM water electrolyser for hydrogen production, Int. J. Hydrogen Energy 34 (3) (2009) 1143–1158.

[35] U.S. Abhishek, P.K. Tewari, V. Anand, Mathematical modelling and dynamics of proton exchange membrane electrolyzer, Int. J. Hydrogen Energy 99 (2025) 189–202.

[36] G. Sakas, P. Rentschler, A. Kosonen, et al., Dynamic mass and energy balance model of a 50 kW proton exchange membrane electrolyzer system, Appl. Energy 382 (2025) 125199.

[37] B. Han, S.M. Steen, J. Mo, et al., Electrochemical performance modeling of a proton exchange membrane electrolyzer cell for hydrogen energy, Int. J. Hydrogen Energy 40 (22) (2015) 7006–7016.

[38] K. Tsamaase, J. Sakala, E. Rakgati, et al., Solar PV module voltage output and maximum power yearly profile using simulink-based model, in: 10th IEEE International Conference on Renewable Energy Research and Applications (ICRERA 2021), 2021, p. 31, https://doi.org/10.1109/ICRERA52334.2021.9598794.

[39] F. Oueslati, HOMER optimization of standalone PV/Wind/Battery powered hydrogen refueling stations located at twenty selected French cities, Int. J. Renew. Energy Develop. 12 (6) (2023) 1070–1090.

[40] F. Oueslati, N. Toumi, Technical feasibility and financial assessment of autonomous hydrogen refuelling stations fully supplied by mixed renewable energy systems for twenty selected sites located in France, Environ. Develop. Sustain. (2024).

[41] N.A.S. Elminshawy, S. Diab, Y.E.S. Yassen, et al., An energy-economic analysis of a hybrid PV/wind/battery energy-driven hydrogen generation system in rural regions of Egypt, J. Storage Mater. 80 (2024) 110256.

[42] F. Gallardo, J. García, A. Monforti Ferrario, et al., Assessing sizing optimality of OFF-GRID AC-linked solar PV-PEM systems for hydrogen production, Int. J. Hydrogen Energy 47 (64) (2022) 27303–27325.

[43] W. Ajeeb, R. Costa Neto, P. Baptista, Life cycle assessment of green hydrogen production through electrolysis: a literature review, Sustain. Energy Technol. Assess. 69 (2024) 103923.

[44] X. Cai, R. Lin, J. Xu, et al., Construction and analysis of photovoltaic directly coupled conditions in PEM electrolyzer, Int. J. Hydrogen Energy 47 (10) (2022) 6494–6507.

[45] K. Yu, Z. Yang, J. Liang, et al., An individual adaptive evolution and regional collaboration based evolutionary algorithm for large-scale constrained multiobjective optimization problems, Swarm Evol. Comput. 95 (2025) 101925.

[46] J. Kennedy, R. Eberhart, Particle swarm optimization; proceedings of the Proceedings of ICNN'95 – International Conference on Neural Networks, F 27 Nov.-1 Dec. 1995, 1995.

[47] Y. Shi, R. Eberhart, A modified particle swarm optimizer; proceedings of the 1998 IEEE International Conference on Evolutionary Computation Proceedings IEEE World Congress on Computational Intelligence (Cat No98TH8360), F 4-9 May 1998, 1998.

[48] J. Zou, L. Tang, Y. Liu, et al., A two-stage direction-guided evolutionary algorithm for large-scale multiobjective optimization, Inf. Sci. 674 (2024) 120719.

[49] Y. Chen, A spectral Hestenes–Stiefel CG algorithm for large-scale unconstrained optimization in image restoration problems, J. Comput. Appl. Math. 470 (2025) 116709.

[50] Z. Hu, X. Nie, H. Sun, et al., Sparse large-scale multi-objective optimization algorithm based on impact factor assistance, Eng. Appl. Artif. Intel. 151 (2025) 110615.

[51] T. Nguyen Duc, K. Goshome, N. Endo, et al., Optimization strategy for high efficiency 20 kW-class direct coupled photovoltaic-electrolyzer system based on experiment data, Int. J. Hydrogen Energy 44 (49) (2019) 26741–26752.

[52] N.A. Kelly, T.L. Gibson, D.B. Ouwerkerk, Generation of high-pressure hydrogen for fuel cell electric vehicles using photovoltaic-powered water electrolysis, Int. J. Hydrogen Energy 36 (24) (2011) 15803–15825.

[53] T.L. Gibson, N.A. Kelly, Optimization of solar powered hydrogen production using photovoltaic electrolysis devices, Int. J. Hydrogen Energy 33 (21) (2008) 5931–5940.

[54] T.L. Gibson, N.A. Kelly, Predicting efficiency of solar powered hydrogen generation using photovoltaic-electrolysis devices, Int. J. Hydrogen Energy 35 (3) (2010) 900–911.

[55] X. Gu, Z. Ying, X. Zheng, et al., Photovoltaic-based energy system coupled with energy storage for all-day stable PEM electrolytic hydrogen production, Renew. Energy 209 (2023) 53–62.